Coupled composition-deformation phase-field method for multicomponent lipid membranes

Chloe M. Funkhouser,[1] Francisco J. Solis,[2] and K. Thornton[1]
[1]*Department of Materials Science and Engineering, University of Michigan, Ann Arbor, Michigan, 48109, USA*
[2]*Department of Integrated Natural Sciences, Arizona State University, Glendale, Arizona, 85069 USA*
(Received 23 February 2007; revised manuscript received 4 May 2007; published 17 July 2007)

We present a method for modeling phase transitions and morphological evolution of binary lipid membranes with approximately planar geometries. The local composition and the shape of the membrane are coupled through composition-dependent spontaneous curvature in a Helfrich free energy. The evolution of the composition field is described by a Cahn-Hilliard-type equation, while shape changes are described by relaxation dynamics. Our method explicitly treats the full nonlinear form of the geometrical scalars, tensors, and differential operators associated with the curved shape of the membrane. The model is applied to examine morphological evolution and stability of lipid membranes initialized in a variety of compositional and geometric configurations. Specifically, we investigate the dynamics of systems which have a lamellar structure as their lowest energy state. We find that evolution is very sensitive to initial conditions; only membranes with sufficiently large lamellar-type compositional perturbations or ripple-type shape perturbations in their initial configuration can deterministically evolve into a lamellar equilibrium morphology. We also observe that rigid topographical surface patterns have a strong effect on the phase separation and compositional evolution in these systems.

DOI: 10.1103/PhysRevE.76.011912 PACS number(s): 87.68.+z, 87.10.+e

I. INTRODUCTION

Multicomponent lipid membranes are versatile systems that play important roles in biological structure and function. They are useful as model systems for biophysical investigations, and have many potential technological applications, especially in connection with biosensors. The interplay of geometric shape and composition is a crucial but common aspect of membranes. In biological processes, composition drives the geometric changes required by protein transport. In model systems, such as giant unilamellar vesicles (GUVs), direct observation of composition and geometry reveal important information about the molecules comprising the membranes.

It has been demonstrated that lipid vesicles with compositions similar to that of cellular membranes exhibit phase separation and have complex phase diagrams [1–8]. Observed phases include liquid, liquid crystalline, and solid states. The possibility of stable microsegregated morphologies such as caplets and lamellae [9] within the ordered phases adds further complexity to the phase diagram. Determination of the full phase diagram that includes thermodynamics and morphology has not yet been fully carried out, even for selected systems.

Various numerical methods have recently been applied to membrane systems, mainly using one of two approaches. The first approach is based on molecular dynamics (MD) simulations that treat each lipid molecule explicitly. MD simulations are useful in investigating the relation between the molecular structure and the membrane properties. For example, lipid-lipid and cholesterol-lipid interactions, which give rise to net cohesiveness and bending rigidity, have been analyzed by this method [10–13]. The second approach is to use continuum-level methods to study dynamical evolution at larger length and time scales. Recent work of Ayton *et al.* [14] employed smooth particle applied mechanics for phase-field models. They found that composition responded to geometrical surface perturbations imposed on the vesicle. A continuum approach based on the representation of a vesicle as a level set has been used by Du *et al.* [15,16] to study complex axis-symmetric shapes.

We present a continuum-level method for modeling phase transition and corresponding morphological evolution of binary lipid membranes with approximately planar geometries. Our model is also a continuum-level model based on Cahn-Hilliard-type dynamics as in [14], but it treats explicitly the full nonlinear form of the geometrical scalars, tensors, and differential operators associated with the curved shape of the membrane. The model is applied to examine morphological evolution and stability of lipid membranes. Dynamical equations for modeling planar membrane systems are presented, as well as the numerical scheme developed to implement these equations. The implementation of the method is validated by accurately reproducing features expected from analytical calculations as discussed later. New aspects of membrane dynamics are also investigated. It is found that the formation of the lowest-energy equilibrium morphological phase, consisting of alternating single-phase lamellae, is kinetically unlikely when the initial state is purely stochastic for the parameter set examined. Although the morphological phase is energetically preferred, the approach to that morphological phase may be difficult as a series of domain coalescence must occur in the process.

II. THEORY

The morphological behavior of homogeneous vesicles and membranes can be quantified by the Helfrich free energy [17]. This free energy is based on a coarse-grained model that treats the membrane as a smooth surface. The spatial shape of the surface can be described by a three-dimensional coordinate function $\mathbf{x}(\mathbf{u})$ that depends on a two-dimensional

coordinate **u** that parametrizes the surface. This model considers the energy cost of bending deformations away from conformations with the spontaneous curvature, i.e., the preferred curvature originating from the molecular shapes and interactions. Nonzero spontaneous curvatures stem from asymmetry between the two surfaces of the membrane. Our model is therefore useful for monolayers, which are intrinsically asymmetric, and bilayers with asymmetry. Asymmetry in bilayers can arise, for example, from differences between the mediums at opposite sides of the membrane, such as unequal concentrations of salt ions and other molecules. In addition, this formulation often includes two Lagrangian multipliers, the surface tension and the pressure, to control the values of the total area of the membrane and the volume enclosed by it, respectively.

The basic Helfrich model can be extended to multicomponent systems [18,19]. In a binary system with components A and B, we consider phase coexistence between two phases, α and β, with majority components A and B, respectively. The concentration of B in these phases is c_α and c_β, respectively; we denote the position-dependent concentration of B simply as c. We introduce a local phase composition function $\phi=(c-c_\beta)/(c_\alpha-c_\beta)$ that takes values between 0 and 1. In the strong segregation limit, when the components are highly immiscible, most of the membrane area is occupied by single-phase regions with compositions of $\phi=0$ or $\phi=1$. In the boundary region between two phases, the composition field smoothly interpolates between these values. Compared to the homogenous case, the energy of the system is modified in two ways: First, each of the phases may have different mechanical properties and, second, it is necessary to describe the immiscibility of the components.

Below, we write all contributions to the energy density and the resulting dynamical equations in covariant form. Specifically, the equations are independent of both the coordinate systems used for the position of the membrane surface and those used to parametrize it. At the end of the section we specialize the resulting equations to a particular type of coordinate system, the Monge gauge.

The modified Helfrich free energy F of a binary membrane can be written as an integral of an energy density H over the surface of the membrane. We decompose the density H into three terms,

$$F = \int H\, dA = \int (H_0 + H_1 + H_2) dA. \tag{1}$$

The first energy density H_0 describes the thermodynamics of the mixture. We use the standard Landau form [20],

$$H_o = \frac{w}{4}\phi^2(1-\phi)^2 + \frac{\zeta^2}{2}\nabla^i\phi\nabla_i\phi, \tag{2}$$

where w defines the barrier height in the double well free energy and ζ sets the energetic penalty for composition gradients. In the absence of other interactions, the minima of the double well potential in the first term produces two phases at $\phi=0$ or $\phi=1$. The second term penalizes the presence of composition gradients. The coefficients w and ζ can be adjusted to describe the strength of the immiscibility with respect to the mechanical properties of the membrane. In this paper, we examine the strong segregation regime, where, for flat systems, the line tension between species can be identified with $\lambda=(w\zeta^2/72)^{1/2}$. The gradient, divergence, and Laplace operators that appear in this formulation act on functions defined only at the surface of the membrane. We use the standard notation of subindices and superindices for contravariant and covariant vectors, respectively, as well as the index summation convention. These indices identify generalized coordinates that parametrize the surface. Explicit expressions for these differential operators are derived by applying the standard techniques used in general relativity. The results are given in covariant form and in the Monge gauge in Appendix A. In the case of a flat membrane, both the covariant and contravariant gradients reduce to the standard form $\nabla_i=(\partial_1,\partial_2)$, where 1, 2 are indices for Cartesian coordinates in the plane.

The second energy density is a modification of the original Helfrich Hamiltonian that describes the mechanical properties of the membrane,

$$H_1 = \frac{\Lambda}{2}p(\phi)(K-C_\alpha)^2 + \frac{\Lambda}{2}[1-p(\phi)](K-C_\beta)^2, \tag{3}$$

which represents the energy penalty for having a curvature that differs from the spontaneous curvature. In this expression, each term is a standard bending energy with bending rigidity Λ and spontaneous curvature C_α or C_β, and we introduce an interpolation function $p(\phi)$ to interpolate the energies in regions that do not correspond to a single phase ($\phi\neq 0,1$), as discussed later. We have written the Helfrich expressions in terms of K, the trace of the curvature tensor K_{ab}, which is equal to twice the mean curvature. We will refer to this quantity as the curvature trace, for short. The curvature trace is related to the mean curvature H_m by $K=2H_m$; we follow the notation used in Ref. [21]. We consider only the case in which the two phases have equal bending rigidities Λ but have different spontaneous curvature values. These values are C_α for the phase with $\phi=1$, and C_β for the phase with $\phi=0$. To interpolate the energy between these values, we use a smooth function $p(\phi)=\phi^3(10-15\phi+6\phi^2)$ that has the property that $p(0)=0$, $p(0.5)=0.5$, $p(1)=1$, and $dp/d\phi|_{\phi=0}=dp/d\phi|_{\phi=1}=0$. This particular form of an interpolation function is obtained by integrating $\phi^2(1-\phi)^2$ [22], which has the form of the double well potential we adopted. However, other choices of interpolating functions satisfying these prescribed properties are equally valid [e.g., $p(\phi)=\phi^2(3-2\phi)$], given that the function is numerically resolved and that the interfacial (interpolated) region is taken to be sufficiently thin. They provide thermodynamic consistency as discussed by Wang *et al.* [22]. While a very simple interpolation function could be considered [$p(\phi)=\phi$ for example], the chosen form has a proper behavior near $\phi=0$ and $\phi=1$ and helps to ensure that the positions of the free energy minima remain at $\phi=0$ and $\phi=1$ for all curvatures outside of interfacial regions. We define a local average of the spontaneous curvature as $C_f=p(\phi)C_\alpha+[1-p(\phi)]C_\beta$.

One more term can be included in the free energy, which is also directly related to the mechanical properties of the membrane. We can write, for example,

$$H_{1b} = \Lambda_R R \tag{4}$$

for the energy density associated with deformations that create a net scalar curvature R ($R=2G$, where G is the Gaussian curvature). As with the coupling to the curvature trace K, we assume the associated bending rigidity Λ_R is the same for all components. For closed membranes the integral of this term is a topological invariant and can be ignored in processes without topological changes. For open membranes it gives rise to nontrivial boundary contributions. In this work, however, we consider membranes with periodic boundary conditions, and thus the net contribution to the free energy from this term is identically zero (as shown in Appendix B). Therefore, we omit this term from the rest of the main text.

We note that this mechanical energy term has a contribution to the magnitude of the line tension, and thus in general the line tension does not have the value given nominally by the well height of the double well free energy and the gradient-energy coefficient appearing in Eq. (2). The change in the line tension is described by the Gibbs adsorption equation [23–25], and the resulting effect is similar to that obtained for surface stress effects in solidification [26]. However, when the interfacial thickness is much smaller than the length scale given by the ratio of the interfacial energy to the bulk energy density, the excess becomes negligible [26–28]. This is because the excess energy resulting from the bulk energy term scales with the interfacial thickness, while the parameters are set such that the line tension is independent of the interfacial thickness. A similar principle applies here. To ensure accuracy, we choose the interfacial thickness to be much smaller than the inverse of the spontaneous curvatures and a length scale given by the approximate ratio of the line tension to the mechanical energy density $\sim\lambda/\Lambda$.

The third term controls the total area of the membrane, and is given simply by a constant surface tension:

$$H_2 = \sigma. \tag{5}$$

The tension σ is an isotropic contribution to the stress tensor that opposes an increase in the membrane area. This term arises from a coarse-graining of cohesive forces between the molecules that form the membrane. Upon integration of this density, we obtain a linear coupling of the tension and the total area of the membrane, A. The tension and the total area are thermodynamically conjugate variables. We choose to work with a thermodynamic ensemble with constant surface tension and variable area due to the ease of developing a mathematical description. In this ensemble, the prescribed tension determines a unique equilibrium value for the total area.

In experiments, the membrane tension is not one of the controlled parameters, but rather it is implicitly determined by other thermodynamic quantities. It is often considered that the complementary ensemble, with fixed area and adjustable tension, is a better approximation of experimentally realizable conditions in which area changes are small even when tension changes are large. This fixed-area ensemble will be investigated elsewhere. Nevertheless, we point out that the fixed-tension ensemble closely approximates a membrane under tension near its equilibrium configuration. In this case, area changes during the evolution toward equilibrium are small and their effect on the dynamics is negligible. We numerically investigate these cases in which the area changes are indeed very small. We show below that the shape equilibrium conditions also imply equilibrium against area changes.

Our model describes both the equilibrium configurations and the dynamical approach to equilibrium of binary membranes. The equilibrium configurations that result from the above free energy are determined from suitable minimization of the functional with respect to shape and local composition. To describe the dynamics of the system, more information is required. We propose a simple dynamical scheme that couples shape deformations and compositional redistribution.

The most general (small) shape deformation of a membrane is a composite of tangential and normal deformations. The normal deformations can be written as $\delta\mathbf{x}=\psi\mathbf{n}$ where $\mathbf{n}$ is the normal unit vector. Tangential deformations can be expressed in terms of local vectors $\mathbf{e}_i$ tangent to the surface as $\delta\mathbf{x}=\psi^i\mathbf{e}_i$ (with contraction over the i indices). For a single component membrane, it has been shown that tangential deformations are equivalent to reparametrizations of the surface and therefore do not generate restorative forces [29]. Thus, the force induced by a deformation can be determined from variations in the normal direction [21]. For a multicomponent membrane, the tangential deformations advecting the composition field induce internal changes of composition and are not equivalent to reparametrizations. In this case, however, equilibrium can be recovered through a combination of normal deformations and compositional redistribution. It is therefore possible to describe the dynamics by considering only normal deformations and diffusion processes, neglecting effects of tangential flows.

The structure of the dynamical equations of a homogeneous membrane that obey the covariant condition has been previously studied by Cai and Lubensky [30]. Among the possible reductions of the full dynamics to a manageable set of variables, they considered a Rouse model without inertial terms. This approximation is still covariant, but neglects inertial terms and tangential forces. The forces generated by deformations of the membrane are then compensated for by friction terms proportional to the normal velocity of the membrane. We adopt this approach to the study of the dynamics of multicomponent systems. The free energy change associated with a normal deformation $\psi\mathbf{n}$ (see Fig. 1) can be written as the integral $\delta F=-\int T\psi\, dA$. T is the generalized force density that couples to the displacement ψ. Expressions for this force are well known for homogeneous membranes. In the case of multicomponent systems, the proper expressions are most easily obtained using the covariant methods of Capovilla *et al.* [21], and are presented explicitly below. The required steps of this derivation are sketched in Appendix B. The normal velocity field is $\mathbf{v}_n=\partial_t\psi\mathbf{n}$, and the friction force opposing the motion is $\mathbf{f}_v=-\mathbf{v}_n/\gamma=-\partial_t\psi\mathbf{n}/\gamma$, where γ is the inverse of the friction coefficient. The dynamical equation is then obtained from the condition $T\mathbf{n}+\mathbf{f}_v=\mathbf{0}$:

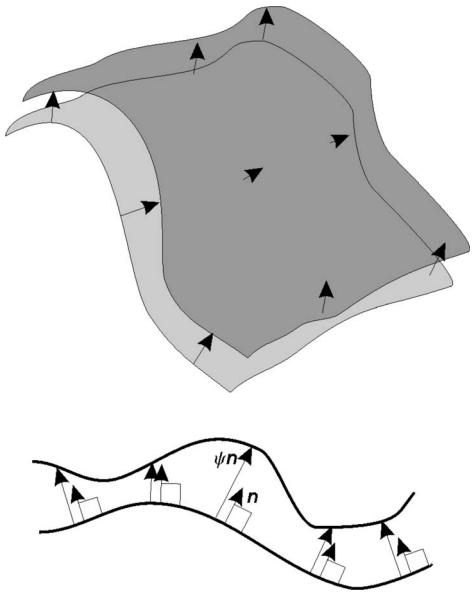

FIG. 1. A schematic illustrating membrane deformations, showing how each point of the membrane can be mapped onto a new point in the deformed membrane located a distance away from its initial location, in the direction of the unit normal vector at that point.

$$\frac{\partial \psi}{\partial t} = \gamma T, \tag{6}$$

$$-T = HK + \Lambda(K - C_f)(R - K^2) - \Lambda\Delta(K - C_f) - \zeta^2 K^{ab}\nabla_a \phi \nabla_b \phi. \tag{7}$$

In this expression, Δ is the Laplace operator and K^{ab} is the curvature tensor (see Appendix A). The shape equation (i.e., the equation governing the morphology of the membrane surface) in equilibrium is simply $T=0$. It is clear that the shape equation of a homogeneous membrane is recovered when the composition field is set to one of the two equilibrium phase values.

We note that in our description of the membrane we consider the tension σ fixed, and thus it is necessary to adjust the area so as to minimize the total energy under this condition. Briefly, normal deformations of the shape induce area changes except in regions where the curvature trace is identically zero (a set of negligible size in most conditions). The deformation of the metric factor is $\delta\sqrt{g} = \delta(dA)/dA = K\psi$ (see Appendix B). Therefore, equilibrium against normal deformations implies equilibrium against area changes. Explicitly, $\delta F = \int(-T\psi)dA = \int -(T/K)\delta\sqrt{g}dA$ and the condition for area equilibrium $T/K=0$ is satisfied when shape equilibrium $T=0$ holds.

The local composition of the membrane is modified both by diffusion processes and advection by tangential displacements. As mentioned above, to obtain a simple effective dynamical scheme we assume that the local composition field evolves by means of diffusional processes. The diffusion is driven by gradients in the chemical potential of the species. For a binary system it is sufficient to consider the diffusion

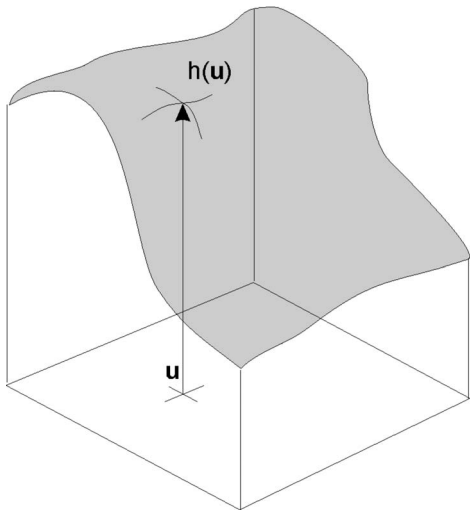

FIG. 2. A schematic illustrating one-to-one projection of the membrane surface onto the background surface. In this case, every shape can be described by a single "height" function $h(\mathbf{u})$.

of just one of the components, say B, which is proportional to ϕ. A chemical potential μ for phase composition is obtained from variation of the free energy with respect to the composition field ϕ, $\delta F = \int dA \mu \delta\phi$. Simple model dynamics are obtained by assuming that the flux j_i transporting scaled composition is proportional to the gradient of the chemical potential $j_i = -M\nabla_i \mu$, where M is an effective mobility, assumed constant throughout this paper. The rate of composition change is then given by $\partial_t \phi = -\nabla^i j_i$. Combining these equations we obtain a Cahn-Hilliard-type dynamics for the composition:

$$\frac{\partial \phi}{\partial t} = M\Delta\mu, \tag{8}$$

$$\mu = \frac{w}{2}\phi(1-\phi)(1-2\phi) - \zeta^2\Delta\phi - \Lambda K p'(\phi)(C_\alpha - C_\beta) + \frac{\Lambda}{2}p'(\phi)(C_\alpha^2 - C_\beta^2). \tag{9}$$

Equilibrium is achieved when the chemical potential becomes uniform so that its gradient is zero. Normal deformations that change the shape leave the composition invariant. It is necessary, however, to consider the change of composition at fixed background points induced by the normal motion; this is considered at the end of this section.

The dynamical equations proposed above can be solved numerically using various methods. Since the dynamics of the shape has been reduced to that of a single scalar variable, it is viable to use the Monge gauge. That is, after setting a fixed geometrical background, we describe the shape of a membrane by specifying its projection onto the background. We require that this projection be one-to-one. These shapes are then described by a single "height" function $h(\mathbf{u})$ as shown in Fig. 2. The dynamical behavior of the system can then be reduced to the time evolution of the composition ϕ and the height h variables. To obtain an explicit numerical

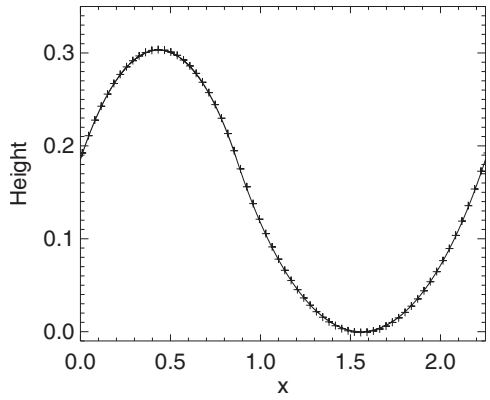

FIG. 3. One-dimensional plot of a cross section of the height profile for a lamellar morphological phase, comparing analytical [31] and simulation results. Line: Analytical result. Symbol: Simulation result.

scheme, it is necessary to write all the geometric invariants and differential operators that appear in our equations in terms of the height.

We consider in this paper only a flat background, useful when the membrane shape can be projected one-to-one onto a plane. The explicit forms of the relevant geometric quantities and operators for this case are presented in Appendix A. To use our dynamical equations in this setting we need to transform the normal deformation rate $\partial\psi/\partial t$ into a change of the height function $\partial h/\partial t$ and to describe the rate of change of the composition at a physical point in terms of the rate of change at a fixed background point.

Let us consider the first problem. The vector normal to the surface $\mathbf{n}$ has components n_z and $n_\parallel$, perpendicular and parallel to the background plane, respectively. The height change rate of a physical point is $dh/dt=(\partial\psi/\partial t)n_z$ while the projection of its velocity onto the background plane is $(\partial\psi/\partial t)n_\parallel$. This projection defines a coordinate s along which the displacement takes place. The displacement advects the height at a rate $(\partial\psi/\partial t)n_\parallel(\partial h/\partial s)$, and we obtain $dh/dt=(\partial\psi/\partial t)n_z=\partial h/\partial t+(\partial\psi/\partial t)n_\parallel(\partial h/\partial s)$. Solving for the local height change and noting $\partial h/\partial s=-n_\parallel/n_z$ and $n_z=1/g^{1/2}$ where $g^{1/2}$ is the area differential, we obtain the relation $\partial h/\partial t=g^{1/2}(\partial\psi/\partial t)$. Our final result is that, in the Monge gauge, the normal deformation dynamics can be written as

$$\frac{\partial h}{\partial t}=\gamma g^{1/2}T. \tag{10}$$

Next, the composition at the point above a background plane point with coordinates $\mathbf{u}$ changes not only due to diffusion but also due to the motion of the surface:

$$\partial_t\phi|_{\mathbf{u}}=\partial_t\phi|_{\text{diff}}+\partial_t\phi|_{\text{ad}},$$

$$\partial_t\phi|_{\text{ad}}=(g^{ij}z_i\nabla_j\phi)\partial_t h. \tag{11}$$

In these expressions z_i is the inner product of the vector normal to the reference plane $\mathbf{z}$ and the basis vectors $\mathbf{e}_i$, $z_i=\mathbf{z}\cdot\mathbf{e}_i$. The derivative $\partial_t\phi|_{\mathbf{u}}$ measures the composition change at fixed background coordinates. The diffusional contribution, $\partial_t\phi|_{\text{diff}}$, is that determined by the Cahn-Hilliard-type dynamics and as given in Eq. (8). The advection term, $\partial_t\phi|_{\text{ad}}$, is determined as follows. A height change rate vector, $\partial_t h\mathbf{z}$, can be decomposed into two vectors, one the normal deformation and the other tangential to the surface. Thus

$$\partial_t h\mathbf{z}=\partial_t\psi\mathbf{n}+\xi^j\mathbf{e}_j. \tag{12}$$

The advection rate in the reference plane is $\partial_t u^i\mathbf{w}_i$. Since $\mathbf{e}_i$ projects onto the unit vector $\mathbf{w}_i$ within the reference plane, we thus have $\xi^i=-\partial_t u^i$, or

$$\partial_t h\mathbf{z}=\partial_t\psi\mathbf{n}-\partial_t u^j\mathbf{e}_j. \tag{13}$$

Taking the inner product of both vectors with the $\mathbf{e}_i$ basis, we obtain $\partial_t hz_i=-\partial_t u^j g_{ij}$. Solving this system we obtain $\partial_t u^j=-g^{ji}z_i\partial_t h$. Since the Lagrangian derivative is related to the Eulerian derivatives by $D\phi/Dt=\partial\phi/\partial t+\partial_t u^i\partial_i\phi$, which is identically zero when only advection is considered, the time derivative of ϕ at a fixed point $\mathbf{u}$ is given by $\partial_t\phi|_{\text{ad}}=-\partial_t u^i\partial_i\phi$, and the expression in Eq. (11) follows.

III. NUMERICAL METHODS

The dynamical scheme presented above for the geometric and compositional changes can be studied numerically in terms of just two fields: the phase composition and height with respect to a background geometry. Orthogonal lattices consisting of 64 by 64 mesh points are used to discretize the composition and height on a computational domain of size 2.25 by 2.25. This cell size was selected to ensure that the lowest energy morphological phase is lamellae. Energy and length scales of the system can be set by the bending rigidity and spontaneous curvature of phase α. Specifically, we measure all energies in units of the bending rigidity Λ, and all lengths in units of the radius of spontaneous curvature of the α phase, C_α^{-1}. The line tension, surface tension, spontaneous curvature of phase β, and compositional area fraction are all independent parameters.

Derivatives are calculated using the finite-difference method, with a second-order centered-differencing scheme

TABLE I. Summary of compositional and geometrical initial conditions used for the simulations.

	Case number			
	1	2	3	4
Composition	Random noise	Random noise and lamellar perturbation	Random noise or no perturbation	Random noise or no perturbation
Geometry	Flat	Flat	Ripple	Fixed ripple

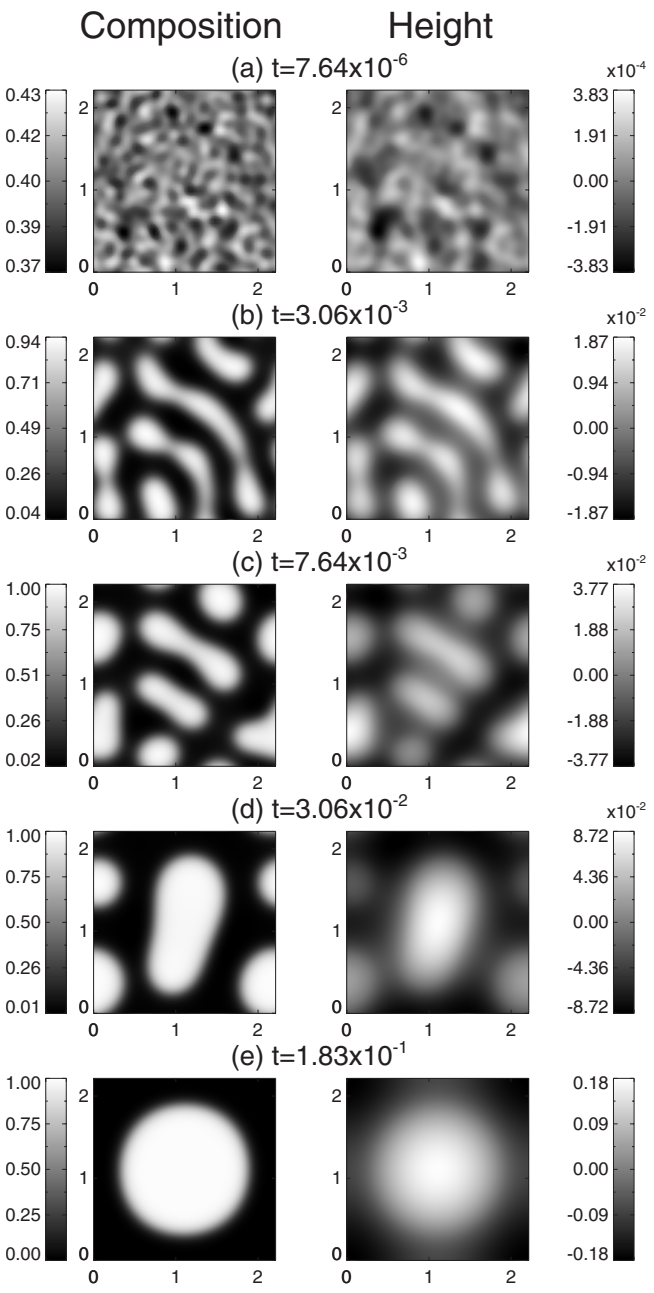

FIG. 4. Contour plots representing the composition and corresponding height fields from a case 1 simulation with $A_{\text{noise}}=5.0\times10^{-2}$. From top to bottom: (a) $t=7.64\times10^{-6}$, (b) $t=3.06\times10^{-3}$, (c) $t=7.64\times10^{-3}$, (d) $t=3.06\times10^{-2}$, and (e) $t=1.83\times10^{-1}$. Without any special perturbation imposed on composition or geometry ($A_{\text{lam}}=A_{\text{ripple}}=0$), all systems evolve similarly to this, forming one round minority-phase domain rather than lamellae.

for spatial derivatives and an explicit time-stepping scheme for time derivatives. The size of the time step is determined to provide numerical stability. Periodicity is imposed on all four boundaries of the computational domain. Mass and surface area are not conserved quantities as we allow deformation of the surface. However, in the cases considered herein, they deviate only minimally from the initial values throughout the evolution (typically, surface area increases by 1–4 %, resulting area fraction changes by 1–4 %). Compositional interfaces are resolved with a minimum of six lattice points to preserve numerical accuracy.

An analytical extended phase diagram (including compositional and morphological phases) presented in [18] indicates a phase with a periodic stripelike arrangement of single-phase domains for a range of concentrations, spontaneous curvatures, line and surface tensions. Harden *et al.* [19] have also studied membranes analytically; their model predicts a similar lamellar phase in systems with low line tension and near-symmetric compositions. In order to further investigate this lamellar phase, we numerically simulate the approach to equilibrium using parameters suggested in [18], defined as follows: $\lambda=0.5$, $\sigma=0.4$, $C_\alpha=1$, $C_\beta=-1$, $\phi_{\text{avg}}=0.4$, and $\Lambda=1$. In addition, we set $w=120, \zeta=\sqrt{0.15}$, $M=1$, and $\gamma=30$. Figure 3 shows a plot of a cross section of the height profile for the lamellar morphological phase, comparing analytical results [31] and the simulation.

IV. DYNAMICS OF PHASE SEPARATION

In the membrane systems investigated, dynamical mechanisms and a competition between multiple driving forces determine the evolution and stable late-stage configurations. These driving forces result from the system's attempt to reduce the sum of surface-tension energy, line-tension energy, and bending energy. In addition, the model includes two pathways for relaxation of nonequilibrium states: the normal deformation of the membrane and diffusional processes that transport material within the membrane. Surface-tension energy is minimized when the membrane is exactly planar; any deformation away from the plane increases the surface-tension energy. The line-tension energy is lowered when the length of the interface between phases is reduced. This can be accomplished both by the process of coarsening, where multiple small domains evolve into fewer, larger domains, and also by domains bulging away from the membrane plane. Bending energy is minimized when single-phase domains are able to adopt the curvature preferred by that phase (the spontaneous curvature). We assume that the diffusion process is slower than normal deformations, and thus the evolution is effectively governed by diffusion, with the geometric shape minimizing the total energy for a given membrane composition.

While there exists a lowest-energy state for a given parameter set, it is unknown whether a phase-separating system will reach such a state or how it evolves toward it. Thus we investigate membrane systems with the same parameter set but different initial conditions. The height profile is initialized in one of two ways: set to zero everywhere (flat) or offset from zero with a small perturbation imposing a periodic ripple structure. Furthermore, in one of the cases where the height profile is initialized with a ripple perturbation, the height is held fixed and not allowed to evolve with time to simulate a membrane supported on a rigid surface possessing a fixed topography. Composition is initialized in one of three ways: set to a constant value everywhere, set with a small amplitude of uniform random noise perturbation centered around an average value ϕ_{avg}, or superposition of this random noise with an additional small perturbation imposing a

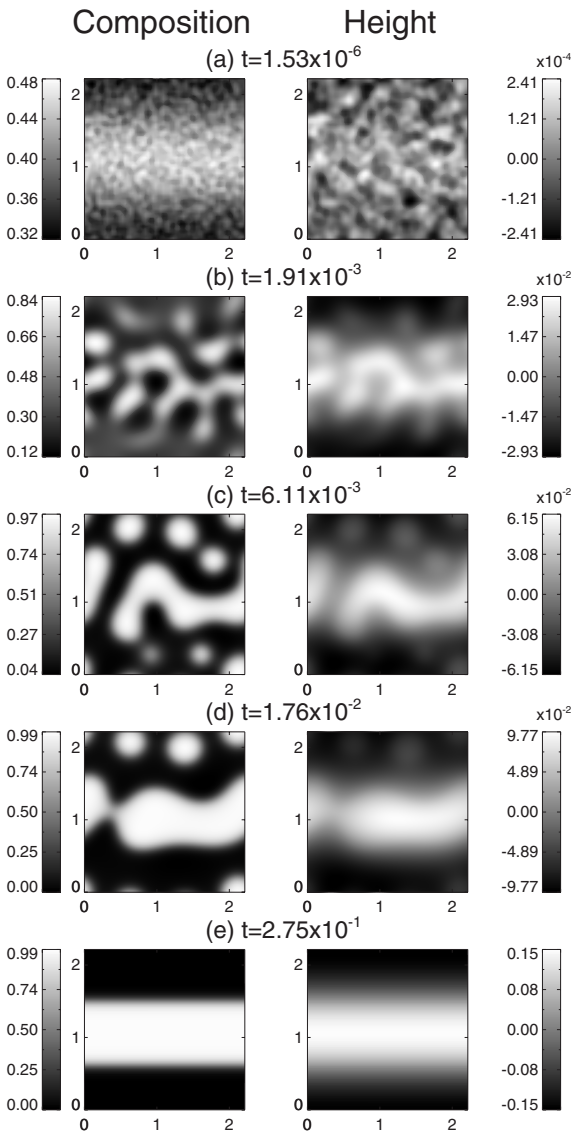

FIG. 5. Contour plots representing the composition and corresponding height fields from a case 2 simulation with $(A_{\text{noise}},A_{\text{lam}})=(5.0\times10^{-2},5.0\times10^{-2})$. From top to bottom: (a) $t=1.53\times10^{-6}$, (b) $t=1.91\times10^{-3}$, (c) $t=6.11\times10^{-3}$, (d) $t=1.76\times10^{-2}$, and (e) $t=2.75\times10^{-1}$. In this case, the perturbation $A_{\text{lam}}=5.0\times10^{-2}$ is sufficient to create a stable lamellar phase by $t=2.75\times10^{-1}$.

periodic lamellar-like structure. A summary of these initial conditions is presented in Table I.

A. Evolution of initially planar membranes

Systems initialized as flat membranes with random noise in the composition field (case 1) will be discussed first. At early stages of the evolution, an initially planar height profile remains nearly flat while the composition changes to the thermodynamic equilibrium values as the mixture separates, forming small domains of minority phase in a matrix of majority phase (see Fig. 4). These small minority-phase domains then coarsen into larger ones, a process driven by the line-tension energy, reducing the total interfacial length. As larger domains form, the height profile responds to the changes in the composition field, and the domains then bulge inward or outward, depending on their spontaneous curvatures. The contour plots in Fig. 4 illustrate the correspondence between local composition and shape. The minority phase α (shown in white in all figures) has a positive spontaneous curvature while the majority phase β (shown in black in all figures) has a negative spontaneous curvature. The curvature effects are evident in the height plots, which show the minority phase bulging outward and the majority phase inward. It should be noted that, in some simulations, the average height slowly deviates from zero during evolution because the dynamics for the height is nonconserving. In these cases, the height values are shifted so that the average height remains at zero.

The process of domains bulging away from the initial membrane plane illustrates the competition among driving forces that governs the compositional and morphological evolution in these membrane systems. Domain bulging increases surface-tension energy, decreases line-tension energy, and could increase or decrease bending energy, depending on the curvature properties possessed by the phases. The bending energy is minimized when domains adopt their spontaneous curvatures; this is generally accomplished by each domain forming a shape resembling either a portion of a half-cylinder or a spherical cap, with a curvature trace equal to the local spontaneous curvature. However, to minimize line-tension energy, a circular domain (or spherical cap) is preferred over a long, cylindrical domain. This is illustrated in Fig. 4(c) at $t=7.64\times10^{-3}$; after coarsening has occurred, minority-phase domains appear in a metastable state with long, partial-cylinder shapes. In the system in Fig. 4, the composition field eventually evolves to a state with a single circular minority-phase domain, as the line-tension energy dominates the energetic competition.

Systems initialized with a small lamellarlike perturbation superimposed on random noise (case 2) will now be discussed. These systems begin in a less random mixture than in case 1, with the lamellar structure visible in the composition plot [Fig. 5(a) at $t=1.53\times10^{-6}$]. Systems are simulated with random-noise amplitudes, A_{noise}, of 5.0×10^{-3}, 1.0×10^{-2}, and 5.0×10^{-2}, along with lamellar perturbations of sinusoidal form with amplitude, A_{lam}, of 5.0×10^{-5}, 5.0×10^{-4}, 5.0×10^{-3}, 1.0×10^{-2}, and 5.0×10^{-2}, with the wavelength equal to the simulation cell size. The system represented in Fig. 5 has $(A_{\text{noise}},A_{\text{lam}})=(5.0\times10^{-2},5.0\times10^{-2})$. In this system, as phase separation occurs, domains of minority phase form, which are initially small and isolated. However, the membrane shape has already responded to the initial compositional lamellar perturbation, forming a ripple structure in the height profile [Fig. 5(b), $t=1.91\times10^{-3}$; Fig. 5(c), $t=6.11\times10^{3}$]. To better visualize the height profile at $t=1.91\times10^{-3}$, it is presented as a surface plot in Fig. 6(a). We note that Fig. 6(a) shows four unit cells (two in each direction) for clarity. Figure 6(b) shows a contour plot of the curvature trace, also at $t=1.91\times10^{-3}$. Once the small domains begin to coarsen, the largest domain oriented along the

axis of the computational domain is able to grow and connect to itself, spanning the computational domain and forming a lamellar structure [Fig. 5(d) at $t=1.76\times10^{-2}$]. The material in the remaining minority-phase domains apart from the largest domain diffuses to the largest lamella domain in order to reduce line-tension energy as well as surface-tension and bending energies. This creates the stable lamellar structure shown in Fig. 5(e) at $t=2.75\times10^{-1}$.

The stable lamellar structure can be obtained when a sufficient amount of lamellar perturbation is imposed on the initial composition field. We find that, regardless of the magnitude of the random noise in the chosen range, a sufficiently large amplitude of perturbation is required in order to create a stable lamellar structure. This amplitude was found to be $A_{\mathrm{lam}}=5.0\times10^{-2}$. However, lamellae do not form deterministically at this amplitude. Different sets of random numbers used to initialize composition occasionally result in very different evolution, as can be observed by comparing Fig. 5 and Fig. 7. Both of these cases are initialized with the same sinusoidal and random-noise amplitudes, although one evolves to lamellae while the other does not. The difference is evident in the fourth row of plots in each of the figures [Fig. 5(d) and Fig. 7(d), at $t=1.76\times10^{-2}$]. As coarsening occurs in the system in Fig. 5, the largest minority-phase domain is able to connect with itself to span the computational domain. Once this connection has been made, a lamellar structure begins to form, which becomes more stable with time. Contrastingly, in the system in Fig. 7, no domains make a connection spanning the entire width of the computational domain, and line-tension energy then drives the minority phase to form round, isolated domains which coarsen. While this illustrates the stochastic nature of the evolution of these systems, lamellae do typically form in cases where $A_{\mathrm{lam}}\geqslant5.0\times10^{-2}$.

The above example indicates that a lamellar structure is able to form only when a single minority-phase domain connects with itself across the simulation cell, as in Fig. 5. As a result of the periodicity we impose on the computational domain, this single connection is all that is necessary to cause the system to evolve into lamellae. However, in a physical system where there is no periodicity, such connections would need to form between all isolated domains in order for a similar lamellar structure to form. Without an imposed periodicity, line-tension energy overcomes the tendency toward a lamellar structure, and the minority phase is expected to form circular domains, as in Fig. 7.

B. Evolution of membranes with initial sinusoidal height perturbations

Systems initialized with a periodic sinusoidal, or ripple, structure imposed on the height profile (case 3) will now be discussed. In these simulations, composition is initialized with $A_{\mathrm{noise}}=0$, 5.0×10^{-4}, 5.0×10^{-3}, or 5.0×10^{-2}, and $A_{\mathrm{lam}}=0$ for all, while the height is initialized to a sinusoidal shape of amplitude $A_{\mathrm{ripple}}=5.0\times10^{-2}$, 1.0×10^{-1}, or 2.0×10^{-1}, with wavelength equal to the size of the simulation cell. In the case where composition is constant ($A_{\mathrm{noise}}=0$), the order parameter is initially set to $\phi_{\mathrm{avg}}=0.4$ everywhere (Fig. 8). In this constant composition case, even at very early times a lamellar structure begins to form in the composition field, although the minimum and maximum values of the order parameter have changed only slightly from $\phi_{\mathrm{avg}}=0.4$. As the system phase separates and the order parameter approaches the equilibrium phase values, the system develops a lamellar structure, with a different periodicity than the ripple that was imposed initially on the height profile [Fig. 8(d) at $t=1.53\times10^{-2}$]. Since the ripple perturbation in the initial height profile is not fixed in time, the height responds to changes in the composition field at later times during phase separation. While a lamellar structure has formed in the system at $t=1.53\times10^{-2}$, it is only metastable, as the minority-phase lamellae merge with each other to form fewer, wider lamellae in order to reduce the line-tension energy. The final configuration of the system we observe is a lamellar structure, which still has a different periodicity than the structure

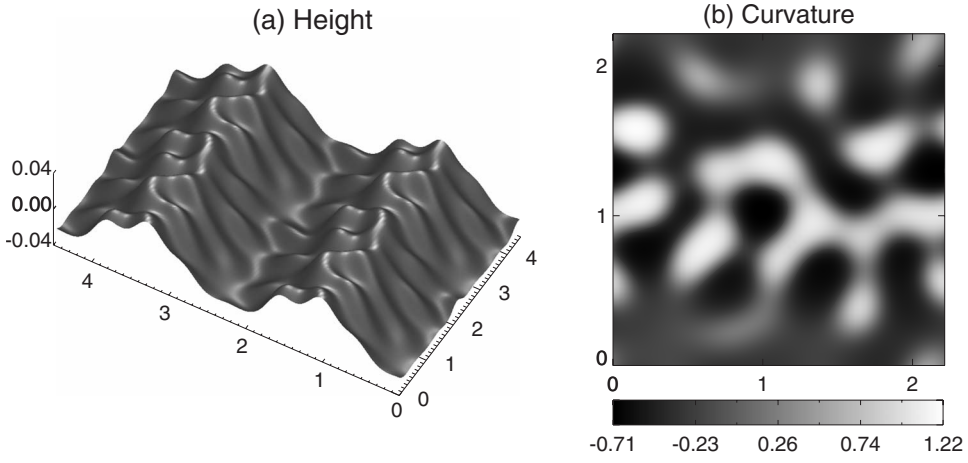

FIG. 6. (a) Surface plot representing membrane geometry and (b) contour plot representing the curvature trace (equal to twice the mean curvature) from a case 2 simulation with $(A_{\mathrm{noise}},A_{\mathrm{lam}})=(5.0\times10^{-2},5.0\times10^{-2})$ at $t=1.91\times10^{-3}$. Note that the surface plot shows four unit cells (two in each direction) for clarity. Compare with the contour plot of height in Fig. 5(b), which presents the same data in two dimensions.

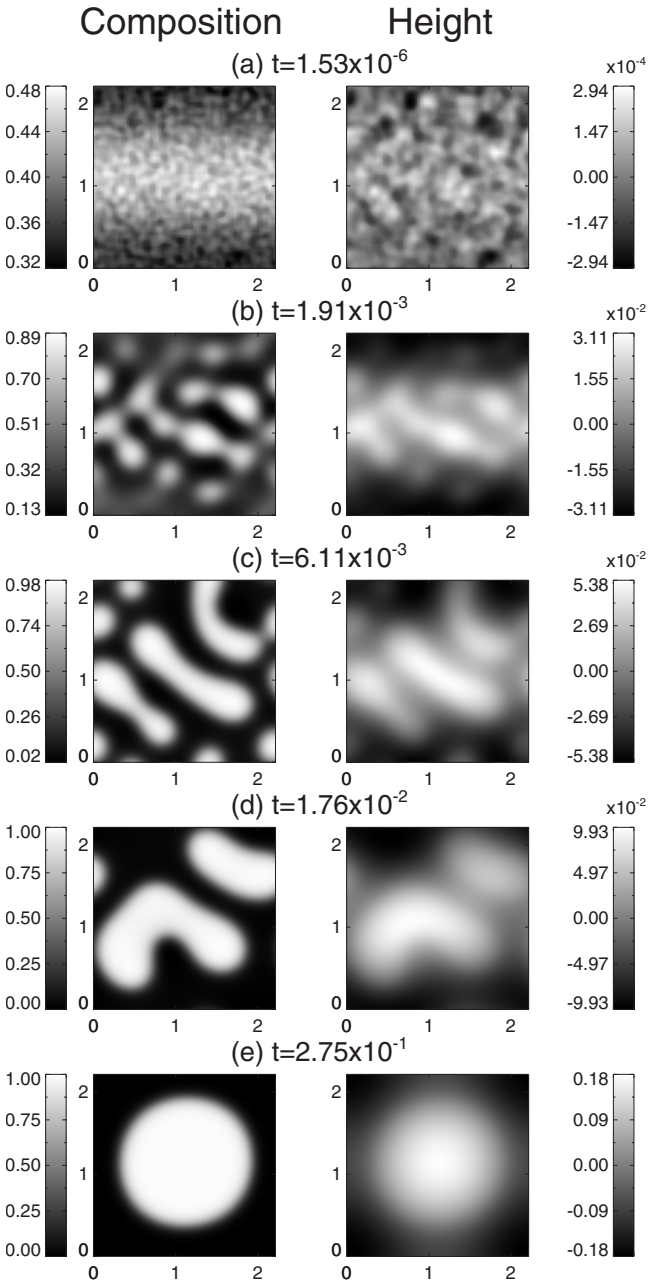

FIG. 7. Contour plots representing the composition and corresponding height fields from a case 2 simulation with $(A_{\text{noise}},A_{\text{lam}})=(5.0\times10^{-2},5.0\times10^{-2})$. From top to bottom: (a) $t=1.53\times10^{-6}$, (b) $t=1.91\times10^{-3}$, (c) $t=6.11\times10^{-3}$, (d) $t=1.76\times10^{-2}$, and (e) $t=2.75\times10^{-1}$. In this case, $A_{\text{lam}}=5.0\times10^{-2}$ is insufficient to create stable lamellae, although case 2 simulations with these parameters do typically create a stable lamellar phase (see Fig. 5). This is one example illustrating how the dynamics and final configurations of these systems are very sensitive to initial conditions.

initialized in the height. While this periodicity is higher in energy than the equilibrium state with the periodicity used for the height initialization, the driving force for lamellae to coarsen is too small to push the system out of this relatively stable configuration, at least in the time scale of simulations we are able to perform.

The results from simulations using $A_{\text{noise}}\neq0$ differ significantly from those using $A_{\text{noise}}=0$. The ripple structure tends to remain in the height profile only until the composition order parameter approaches the equilibrium phase values as the system phase separates [Fig. 9(c) at $t=3.82\times10^{-3}$]. The random noise imposed in the composition determines roughly where domains of the two phases will form. Unlike in the $A_{\text{noise}}=0$ case, the random noise causes the composition to initially deviate from the periodicity of the height profile, and compact minority-phase domains form in all regions of the membrane. The height profile then follows the evolving composition, losing all of the ripple structure it initially possessed. The system then evolves just as the case 1 systems do, eventually forming one round minority-phase domain. In one case 3 simulation, where $(A_{\text{noise}},A_{\text{ripple}})=(5.0\times10^{-3},2.0\times10^{-1})$, the evolution is similar to the $A_{\text{noise}}=0$ simulation (Fig. 8). Since A_{noise} is small, the relatively large height perturbation is able to impose a lamellar structure before the height begins to follow the phase separation, and therefore the lamellar phase forms. In general, however, if a ripple perturbation is imposed only as the initial condition, it is insufficient to drive the system to form a stable lamellar morphological phase, unless the composition is nearly uniform.

C. Evolution of membranes supported on rigid surfaces with a sinusoidal height profile

Systems where the height is fixed with a periodic ripple structure throughout the entire evolution will now be discussed (case 4). In these simulations, $A_{\text{noise}}=0$, 5.0×10^{-2}, 1.0×10^{-1}, 2.0×10^{-1}, or 3.0×10^{-1}, and $A_{\text{lam}}=0$, while $A_{\text{ripple}}=1.0\times10^{-2}$, 1.5×10^{-2}, 2.0×10^{-2}, 2.5×10^{-2}, 3.0×10^{-2}, 4.0×10^{-2}, 5.0×10^{-2}, or 6.0×10^{-2}. The $A_{\text{noise}}=0$ simulation (Fig. 10) initially behaves very similarly to case 3 with $A_{\text{noise}}=0$ (Fig. 8). In both cases, minority-phase lamellae form in the composition plot as the system phase separates, with a different periodicity than the initial ripple in the height profile. Very quickly, the lamellae widen and merge to reduce line-tension energy. Finally, unlike the case 3 $A_{\text{noise}}=0$ simulation, the remaining lamellae merge together to match the periodicity of the fixed ripple structure in the height profile. These $A_{\text{noise}}=0$ case 4 simulations evolved to lamellae for the entire range of ripple amplitudes investigated.

In the cases where composition begins with random noise [Fig. 11, $(A_{\text{noise}},A_{\text{ripple}})=(5.0\times10^{-2},5.0\times10^{-2})$], the evolution resembles Fig. 5 where stable lamellae form in case 2 simulations. In both of these cases, the presence of a ripple in the height profile during phase separation causes single-phase domains to form in locations which best satisfy their spontaneous curvatures. This means that the domains conform to the ripple shape of the membrane, forming lamellae in the composition profile. However, there is a threshold value of A_{ripple} for each amplitude of random noise, below which lamellae do not form. The final equilibrium state that is reached in these cases is a single circular domain within the periodic simulation box, positioned on the region of positive curvature of the fixed ripple structure. The results are summarized in Table II. The general trend of the tabulated

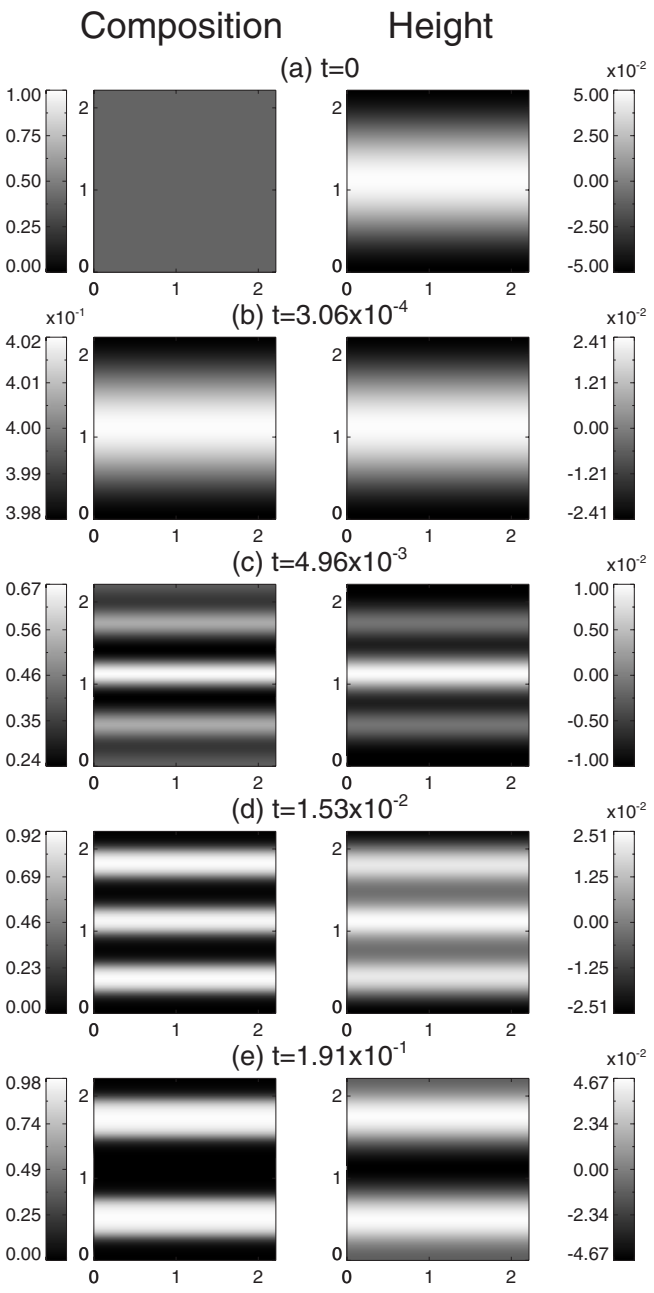

FIG. 8. Contour plots representing the composition and corresponding height fields from a case 3 simulation with $(A_{\text{noise}}, A_{\text{ripple}}) = (0, 5.0 \times 10^{-2})$. From top to bottom: (a) $t=0$, (b) $t = 3.06 \times 10^{-4}$, (c) $t = 4.96 \times 10^{-3}$, (d) $t = 1.53 \times 10^{-2}$, and (e) $t = 1.91 \times 10^{-1}$. As the system phase separates, domains of the two phases form where their spontaneous curvatures are best satisfied. However, the height evolution follows the compositional evolution, and consequently the final lamellar phase we observe attains a different periodicity than the initial ripple.

results is that membranes with a higher amplitude of random noise in composition require a larger ripple amplitude to induce a lamellar structure. Overall, a membrane initially having either a uniform composition or random mixture, resting on a surface that is fixed with a sufficiently large ripple amplitude will, after phase separation, conform its composition profile to match the height profile and form a lamellar morphological phase. Thus we find that topographical patterns with sufficiently large amplitude have a strong influence on the morphological evolution in these systems.

V. CONCLUSIONS

In this paper, we examined phase separation in lipid membranes using a coupled composition-deformation phase-field method, which utilizes the techniques developed in general relativity. We focused on a system that has a lamellar morphology as the lowest energy state. We find that, for the membrane system investigated, the final configuration (morphological phase) is highly sensitive to initial conditions. When there is no initial lamellar-type or ripple-type perturbation, the lamellar morphological phase is not observed. In initially planar systems, we show that lamellae form only when an initial compositional perturbation possessing both the correct symmetry and periodicity with sufficiently large amplitude is imposed. Therefore, it is unlikely that a lamellar structure would form spontaneously from a random lipid mixture on a flat background even if it possesses the lowest energy. Similarly, a sinusoidal ripple perturbation initially imposed on the height that is allowed to evolve is insufficient to induce the lamellar state when random fluctuations in composition exist. Lamellae form in this case only when the composition is initially nearly uniform ($A_{\text{noise}} \approx 0$). Typically, as isolated single-phase domains form from the compositional random fluctuations, the height profile follows composition, and the ripple perturbation that had initially been imposed in the height dissipates. Although the lowest-energy state for the given parameter set is the lamellar state, the dynamics of their formation have specific symmetry requirements that are, in systems with random fluctuations, rarely met. Contrastingly, for a membrane with a rigid sinusoidal ripple structure of sufficiently large amplitude, lamellae will form regardless of the initial conditions in composition. Thus we find that rigid topographical surface patterns have a strong effect on the phase separation and compositional evolution in these systems.

The theory and numerical methods presented in this article provide a model for coupled composition-deformation phase decomposition that occurs in lipid membrane systems. Extension and variations of this model can easily be developed using the methods described herein. For example, we will consider a composition-dependent bending rigidity. This is beyond the scope of this paper, and thus will be investigated elsewhere. However, the model does have limitations. As discussed earlier, the model is based on a constant surface tension ensemble, and the area is allowed to change. Therefore the simulations are limited to systems that do not exhibit substantial area changes during evolution. Also, certain membrane phenomena such as bud formation and vesiculation cannot be simulated within this approach, as a continuous background for projection of the full membrane cannot be defined. We are currently working to improve the model in order to address these limitations and extend its applications. Extending the model to other background geometries such as a spherical background would enable simulations of membrane systems possessing different topologies, including GUVs and mammalian plasma membranes.

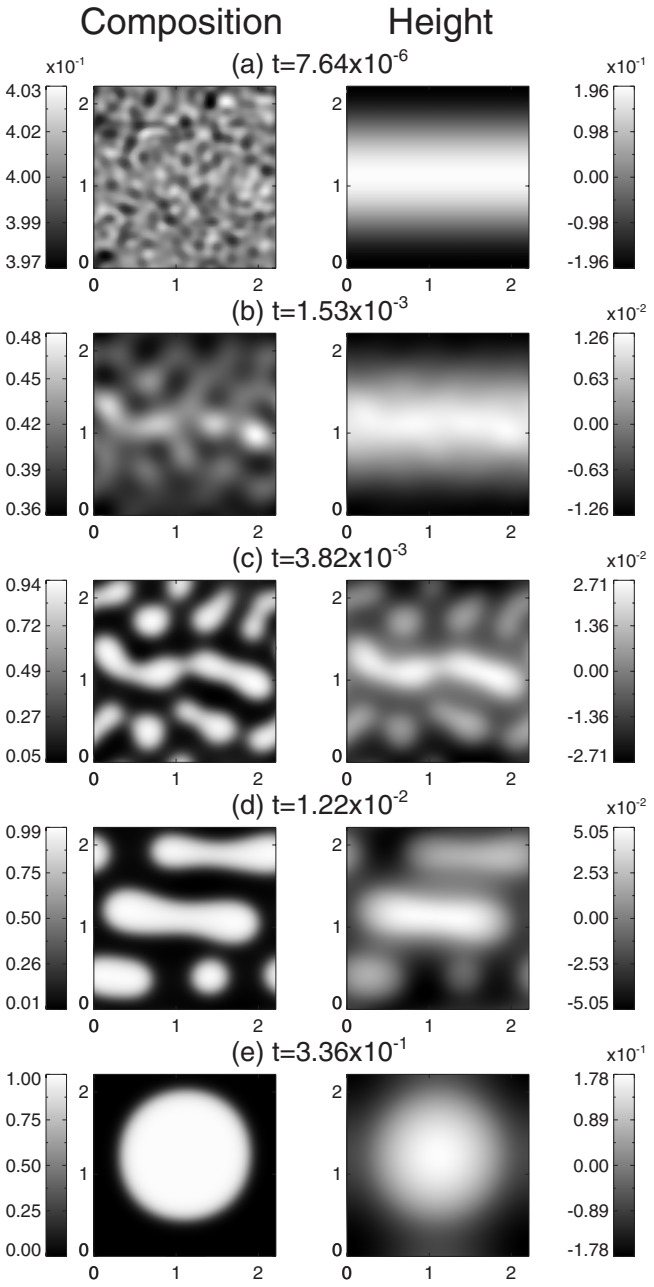

FIG. 9. Contour plots representing the composition and corresponding height fields from a case 3 simulation with $(A_{\text{noise}}, A_{\text{ripple}}) = (5.0 \times 10^{-3}, 2.0 \times 10^{-1})$. From top to bottom: (a) $t = 7.64 \times 10^{-6}$, (b) $t = 1.53 \times 10^{-3}$, (c) $t = 3.82 \times 10^{-3}$, (d) $t = 1.22 \times 10^{-2}$, and (e) $t = 3.36 \times 10^{-1}$. As the system phase separates, the ripple structure is disappearing [(b)–(d): $t = (1.53 \times 10^{-3}) - (1.22 \times 10^{-2})$] because the height evolution follows the compositional evolution that is dictated by the initial random noise. Therefore, no lamellae form and the system evolves to a single, round minority-phase domain.

ACKNOWLEDGMENTS

We gratefully acknowledge the financial support from the UM Office of Vice President of Research and UM startup fund, as well as C. Funkhouser's NSF financial support. We also thank Jemal Guven, Riccardo Capovilla, and Michael Mayer for insightful discussions during the preparation of this work.

APPENDIX A: GEOMETRIC INVARIANTS AND DIFFERENTIAL OPERATORS IN THE MONGE GAUGE

As shown in Fig. 2, the Monge gauge describes a surface by a single function h, the height over a reference plane. This description can be made global when there is a plane onto which the projection is one-to-one, and the transformation between the respective tangent spaces is nonsingular; we consider only this case. All geometric invariants, vectors, tensors, and differential operators can be explicitly written as functions and operators acting in the reference plane. This appendix provides these expressions for the objects used in the body of this article.

A point within the surface is described by its Cartesian coordinates $\mathbf{x} = (x_1, x_2, x_3)$. A point in the reference plane has coordinates $\mathbf{u} = (u_1, u_2)$. We can select these coordinate systems so that $\mathbf{u}$ lies in the $x_3 = 0$ plane, and make the identifications $u_1 = x_1$, and $u_2 = x_2$. The third coordinate of a point on the surface is then $x_3 = h(u_1, u_2)$, and

$$\mathbf{x} = [u_1, u_2, h(u_1, u_2)]. \tag{A1}$$

We label the unit vectors in the reference plane as $\mathbf{w}_1 = (1,0,0)$, and $\mathbf{w}_2 = (0,1,0)$. These are projections of two vectors $\mathbf{e}_1, \mathbf{e}_2$ tangent to the surface. The components of these vectors are

$$\mathbf{e}_1 = \left(1, 0, \frac{\partial h}{\partial u_1}\right) = (1, 0, \partial_1 h), \tag{A2}$$

$$\mathbf{e}_2 = \left(0, 1, \frac{\partial h}{\partial u_2}\right) = (0, 1, \partial_2 h). \tag{A3}$$

In the second expression for each vector we use the shorthand $\partial_i h$ for the partial derivatives of h with respect to u_i.

We next define a number of objects that reflect the geometric properties of the surface. These objects are vectors and tensors based on the two-dimensional space tangent to the surface. Vectors in the Cartesian three-dimensional space are typesetted, as above, in bold variables. On the other hand, vectors and tensors within the surface are identified by their explicit indices. For example, the metric tensor below g_{ij} is a rank two tensor in the tangent space, and each of its indices takes only the values 1 and 2. Note that we use mixed objects, such as the basis pair $\mathbf{e}_i = (\mathbf{e}_1, \mathbf{e}_2)$. Each entry is a vector in three-dimensional space, but the pair behaves as a vector within the surface consisting of two vectors and, as such, is identified by its index i.

The magnitudes and inner products of the vectors $\mathbf{e}_i$ form the metric tensor $g_{ij} = \mathbf{e}_i \cdot \mathbf{e}_j$. Its components are

$$g_{ij} = \begin{pmatrix} \mathbf{e}_1 \cdot \mathbf{e}_1 & \mathbf{e}_1 \cdot \mathbf{e}_2 \\ \mathbf{e}_2 \cdot \mathbf{e}_1 & \mathbf{e}_2 \cdot \mathbf{e}_2 \end{pmatrix} = \begin{pmatrix} 1 + (\partial_1 h)^2 & (\partial_1 h)(\partial_2 h) \\ (\partial_1 h)(\partial_2 h) & 1 + (\partial_2 h)^2 \end{pmatrix}. \tag{A4}$$

The determinant of the metric tensor will be denoted by g:

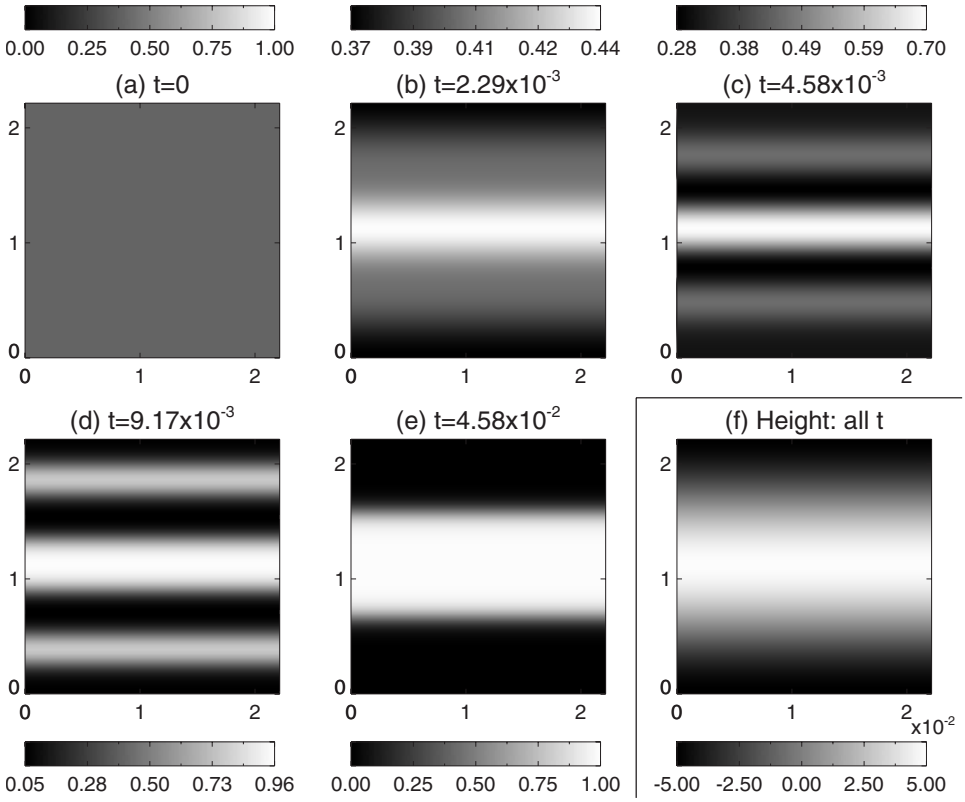

FIG. 10. Contour plots representing composition and height fields for a case 4 simulation, with $(A_{\text{noise}}, A_{\text{ripple}}) = (0, 5.0 \times 10^{-2})$. From top to bottom, left to right: Composition at (a) $t=0$, (b) $t=2.29\times10^{-3}$, (c) $t=4.58\times10^{-3}$, (d) $t=9.17\times10^{-3}$, and (e) $t=4.58\times10^{-2}$; (f) height at all t. The fixed ripple geometry, simulating a membrane on a rigid patterned surface, causes the two phases to form where their spontaneous curvatures are best satisfied, creating a lamellar morphology.

$$g = |g_{ij}| = (1 + \partial_1 h^2 + \partial_2 h^2). \tag{A5}$$

It is also useful to determine the inner product of the unit vector normal to the reference plane $\mathbf{z}=(0,0,1)$ with the vectors tangent to the surface:

$$(z_1, z_2) = (\mathbf{e}_1 \cdot \mathbf{z}, \mathbf{e}_2 \cdot \mathbf{z}) = (\partial_1 h, \partial_2 h). \tag{A6}$$

The matrix inverse g^{ij} of the metric tensor g_{ij} is used to raise indices of vectors and tensors in the standard manner. Its components are

$$g^{ij} = \frac{1}{g}\begin{pmatrix} 1 + (\partial_2 h)^2 & -(\partial_1 h)(\partial_2 h) \\ -(\partial_1 h)(\partial_2 h) & 1 + (\partial_1 h)^2 \end{pmatrix}. \tag{A7}$$

The unit vector normal to the surface $\mathbf{n}$ is obtained by the normalized cross product:

$$\mathbf{n} = \frac{\mathbf{e}_1 \times \mathbf{e}_2}{|\mathbf{e}_1 \times \mathbf{e}_2|} = \frac{1}{\sqrt{g}}(-\partial_1 h, -\partial_2 h, 1). \tag{A8}$$

The curvature tensor K_{ij} is defined as the projection along the normal $\mathbf{n}$ of the derivative of the vector $\mathbf{e}_j$ in the i direction:

$$K_{ij} = -\begin{pmatrix} \mathbf{n} \cdot \partial_1 \mathbf{e}_1 & \mathbf{n} \cdot \partial_1 \mathbf{e}_2 \\ \mathbf{n} \cdot \partial_2 \mathbf{e}_1 & \mathbf{n} \cdot \partial_2 \mathbf{e}_2 \end{pmatrix} = -\frac{1}{\sqrt{g}}\begin{pmatrix} \partial_{11} h & \partial_{12} h \\ \partial_{21} h & \partial_{22} h \end{pmatrix}. \tag{A9}$$

We obtain the two invariants of this tensor, its covariant trace and determinant. The curvature trace is $K = g^{ij} K_{ij}$, and the mean curvature is $H_m = K/2$. The determinant of the tensor gives the scalar curvature R, and the Gaussian curvature G, $G = R/2 = (K^2 - K^{ij} K_{ij})/2$. In the Monge gauge these read

$$K = -\frac{1}{\sqrt{g}}(\partial_{11} h + \partial_{22} h) + \frac{1}{\sqrt{g^3}}[(\partial_1 h)^2 \partial_{11} h + 2\partial_1 h \partial_2 h \partial_{12} h + (\partial_2 h)^2 \partial_{22} h], \tag{A10}$$

$$R = \frac{2}{g^2}[\partial_{11} h \partial_{22} h - (\partial_{12} h)^2]. \tag{A11}$$

To obtain directional derivatives, it is necessary to use information about the derivatives of the vectors defining the local frame on the surface. This information is contained in the Christoffel symbols $\Gamma^i_{jk} = g^{im} \mathbf{e}_m \cdot \partial_j \mathbf{e}_k$. We can present the components of the symbols as the entries of two matrices, one for each value of the upper index:

$$\Gamma^1_{jk} = \frac{\partial_1 h}{g}\begin{pmatrix} \partial_{11} h & \partial_{12} h \\ \partial_{21} h & \partial_{22} h \end{pmatrix}, \tag{A12}$$

$$\Gamma^2_{jk} = \frac{\partial_2 h}{g}\begin{pmatrix} \partial_{11} h & \partial_{12} h \\ \partial_{21} h & \partial_{22} h \end{pmatrix}. \tag{A13}$$

We use several differential operators. A basic quantity is the gradient $\nabla_i f$ of a scalar function f. Its components are

$$\nabla_i f = (\partial_1 f, \partial_2 f). \tag{A14}$$

Note that this vector is attached to the surface and is specified by just two components. Energy terms of free energy

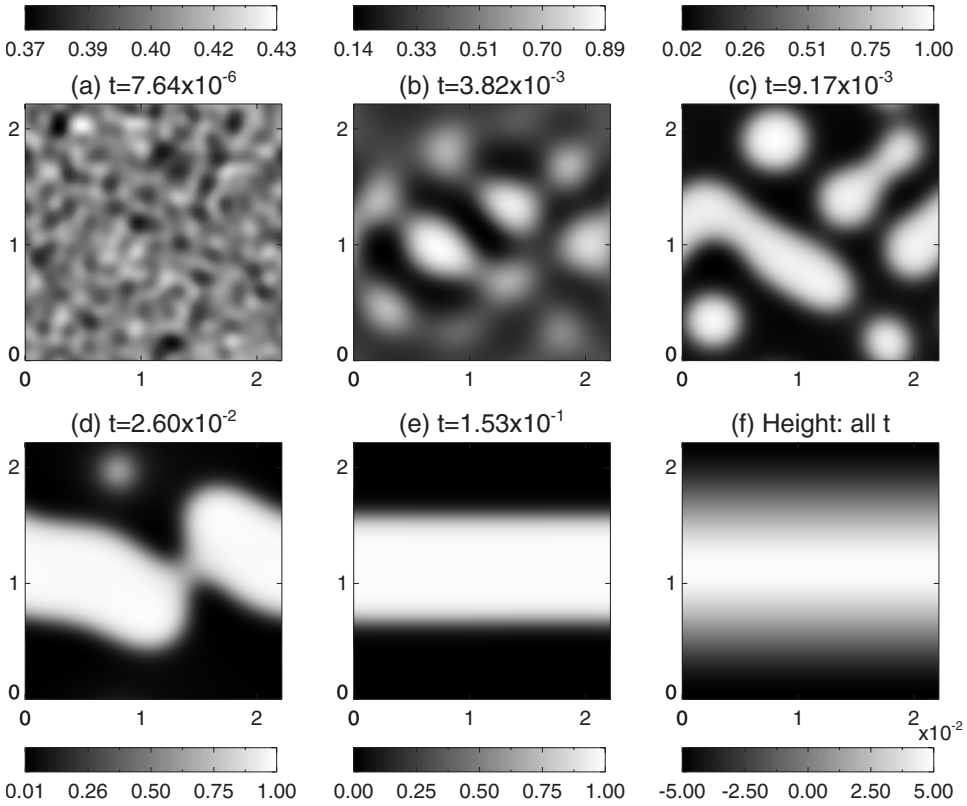

FIG. 11. Contour plots representing composition and height fields for a case 4 simulation with $(A_{\text{noise}}, A_{\text{ripple}}) = (5.0 \times 10^{-2}, 5.0 \times 10^{-2})$. From top to bottom, left to right: Composition at (a) $t = 7.64 \times 10^{-6}$, (b) $t = 3.82 \times 10^{-3}$, (c) $t = 9.17 \times 10^{-3}$, (d) $t = 2.60 \times 10^{-2}$, and (e) $t = 1.53 \times 10^{-1}$; (f) height at all t. The fixed ripple geometry has amplitude above the threshold for lamellae formation, and therefore the two phases form where their spontaneous curvatures are best satisfied, despite the initial compositional fluctuation.

functionals typically involve the magnitude of this vector, $\nabla^i f \nabla_i f = g^{ij} \nabla_i f \nabla_j f$. We obtain

$$\nabla^i f \nabla_i f = \frac{1}{g}\{[1 + (\partial_2 h)^2](\partial_1 f)^2 - 2\partial_1 h \partial_2 h \partial_1 f \partial_2 f + [1 + (\partial_1 h)^2] \times (\partial_2 f)^2\}. \tag{A15}$$

The contraction of the gradient with the curvature tensor $K^{ij} \nabla_i f \nabla_j f$ is much more complicated and we simply state its construction in terms of predefined terms. Due to the symmetry of our metric tensor under transposition, the components of the contravariant curvature can be calculated through a multiple matrix multiplication:

$$K^{ij} = \begin{pmatrix} g^{11} & g^{21} \\ g^{12} & g^{22} \end{pmatrix} \begin{pmatrix} K_{11} & K_{12} \\ K_{21} & K_{22} \end{pmatrix} \begin{pmatrix} g^{11} & g^{12} \\ g^{21} & g^{22} \end{pmatrix}. \tag{A16}$$

In turn, the desired contraction is

$$K^{ij} \nabla_i f \nabla_j f = (\partial_1 f \ \partial_2 f) \begin{pmatrix} K^{11} & K^{12} \\ K^{21} & K^{22} \end{pmatrix} \begin{pmatrix} \partial_1 f \\ \partial_2 f \end{pmatrix}. \tag{A17}$$

TABLE II. Threshold values of A_{ripple} for lamellae formation with respect to A_{noise} for case 4 simulations.

A_{noise}	Interval containing threshold of A_{ripple}
5.0×10^{-2}	$[1.0 \times 10^{-2}, 1.5 \times 10^{-2}]$
1.0×10^{-1}	$[1.5 \times 10^{-2}, 2.0 \times 10^{-2}]$
2.0×10^{-1}	$[1.5 \times 10^{-2}, 2.0 \times 10^{-2}]$
3.0×10^{-1}	$[2.0 \times 10^{-2}, 2.5 \times 10^{-2}]$

The gradient of a vector is defined as $\nabla_i v_j = \partial_i v_j - \Gamma^k_{ij} v_k$. Using this result, the Laplacian of a scalar, defined as $\Delta f = \nabla^i \nabla_i f = g^{ij} \nabla_i \nabla_j f$ is given by

$$\Delta f = g^{11}\partial_{11} f + 2g^{12}\partial_{12} f + g^{22}\partial_{22} f - (g^{11}\Gamma^1_{11} + 2g^{12}\Gamma^1_{12} + g^{22}\Gamma^1_{22})\partial_1 f - (g^{11}\Gamma^2_{11} + 2g^{12}\Gamma^2_{12} + g^{22}\Gamma^2_{22})\partial_2 f, \tag{A18}$$

where we have again used the symmetry of the metric tensor.

APPENDIX B: VARIATIONS WITH RESPECT TO NORMAL DEFORMATIONS

Expressions for the changes in the values of geometric quantities and operators induced by normal deformations of the surface have been summarized in Ref. [21]. We briefly overview some of these results and use them to derive the explicit expression for the normal force density T.

For a small deformation of the form $\delta \mathbf{x} = \psi \mathbf{n}$, the induced deformation for the tangent vector basis $\mathbf{e}_a = \partial_a \mathbf{x}$ is given to the first order by:

$$\delta \mathbf{e}_a = \partial_a (\psi \mathbf{n}) = (\nabla_a \psi)\mathbf{n} + \psi K_{ab} g^{bc} \mathbf{e}_c, \tag{B1}$$

where the second term is obtained from the relation $\partial_a \mathbf{n} = K_{ab} g^{bc} \mathbf{e}_c$. Since the metric can be expressed in terms of the basis vectors, its deformation is now calculated as

$$\delta g_{ab} = 2K_{ab}\psi. \tag{B2}$$

As a consequence, the change in the differential area element is

$$\delta dA = K\psi dA. \tag{B3}$$

The deformation of the normal vector $\mathbf{n}$ is obtained from the rules for the change of the tangential basis, and the properties $\mathbf{e}_a \cdot \mathbf{n} = 0$ and $\mathbf{n} \cdot \mathbf{n} = 1$:

$$\delta \mathbf{n} = -(\nabla_a \psi) g^{ab} \mathbf{e}_b. \tag{B4}$$

With this result, the change in the curvature tensor can be obtained as

$$\delta K_{ab} = -\nabla_a \nabla_b \psi + K_{ac} K_b^c \psi. \tag{B5}$$

From this last expression it is possible to obtain one of the key results required for our model. The variation of curvature trace K is

$$\delta K = -\Delta \psi + (R - K^2)\psi. \tag{B6}$$

The variation of the scalar curvature has two components that we write as

$$\delta R = -KR\psi + 2\nabla_a [(K^{ab} - g^{ab}K)\nabla_b \psi]. \tag{B7}$$

We note that the second term is a divergence that can be integrated out to a boundary term and does not contribute to the bulk equations. These boundary terms are discussed at the end of this appendix. On the other hand, we use the first term to evaluate the bulk variation of the integrand $R\,dA$. We have

$$\begin{aligned} \delta (R\,dA)|_{\text{bulk}} &= -KR\psi\,dA + R\delta(dA) \\ &= -KR\psi\,dA + R\psi K\,dA = 0. \end{aligned} \tag{B8}$$

Thus the scalar curvature term can only produce boundary contributions.

The last result needed is the variation of the gradient term $\nabla^a \phi \nabla_a \phi = g^{ab} \nabla_a \phi \nabla_b \phi$. The deformation leaves the partial derivatives that form the gradient unchanged. The deformation of the contravariant form of the metric is $\delta g^{ab} = -g^{ac} g^{bd} \delta g_{cd} = -2K^{ab}\psi$. We thus obtain

$$\delta\left(\frac{1}{2}\nabla^a \phi \nabla_a \phi\right) = -K^{ab}\psi \nabla_a \phi \nabla_b \phi. \tag{B9}$$

We can now determine the form of the normal force defined by $\delta F = -\int T\psi\,dA$, for small normal deformations of the form $\delta \mathbf{x} = \psi \mathbf{n}$. We omit all the contributions of the scalar curvature terms as they ultimately cancel out when they are gathered together. First we note that the change induced in the area differential produces a term proportional to the free energy density:

$$\delta F = \int [H\delta(dA) + \delta H\,dA] = \int (HK\psi + \delta H) dA. \tag{B10}$$

Next, we calculate the terms arising from variations of the free energy density. The only change in H_0 occurs within terms that couple to the geometry, namely, the gradient terms:

$$\delta H_0 = -\zeta^2 K^{ab} \psi \nabla_a \phi \nabla_b \phi. \tag{B11}$$

The change in the second term, H_1, is obtained from variations of terms proportional to K^2 and K. The variation of these terms is their derivatives with respect to K multiplied by δK. The Laplacian acting on the normal deformation can be twice integrated by parts to remove any derivatives of ψ from our expression. We then obtain $\delta H_1 = -\psi\Delta(\partial H_1/\partial K) + (\partial H_1/\partial K)(R - K^2)\psi$. Explicitly,

$$\delta H_1 = \Lambda\psi(K - C_f)(R - K^2) - \Lambda\psi\Delta(K - C_f). \tag{B12}$$

There are no contributions from the H_2 term, i.e., $\delta H_2 = 0$. Collecting the variations of the area differential and of the free energy densities we obtain

$$-T\psi = HK\psi + \delta H_0 + \delta H_1. \tag{B13}$$

By factorizing the deformation field ψ on both sides of this equation, we obtain Eq. (7) in the main text for the normal force density T.

The normal variations of several terms of the free energy, such as the scalar curvature, produce bulk divergence terms. The divergence theorem in curved manifolds states that the integral of a divergence over a surface M can be recast as a line integral over the perimeter of the surface ∂M [32]. The integrand is the vector density normal to the boundary and tangent to the membrane. The net boundary contribution is

$$\int_M [\nabla_a E^a] dA = \int_{\partial M} \mathbf{E} \cdot \mathbf{n}\,ds, \tag{B14}$$

where $\mathbf{E}$ is the three-dimensional vector defined by the vector components E^a within the surface, and $\mathbf{n}$ is a unit vector normal to the perimeter but tangent to the surface. Since we impose periodic boundary conditions and both the surface coordinates and composition are smooth functions, the corresponding points at opposite edges of the simulation cell have opposite normal directions but equal vector densities. Their contributions therefore cancel:

$$\int_{\partial M} \mathbf{E} \cdot \mathbf{n}\,ds = 0. \tag{B15}$$

This fact holds regardless of the origin of the bulk divergence. In the case of the scalar curvature, however, it is noteworthy that no deformation affects the value of the scalar-Gaussian curvature contribution to the free energy within the simulation cell—its value is a constant—as long as no topological changes occur. As mentioned in the main text, we do not allow topological changes in our simulation, and thus the scalar curvature term in the free energy can be excluded from our analysis without altering the results. Finally, we note that for any surface configuration satisfying the Monge condition, it is possible to arrive at such configurations starting from a flat surface. Since the scalar or Gaussian curvature of the flat surface is zero, it remains zero for any other conformation:

$$\int_{\text{cell}} R\,dA = 0. \tag{B16}$$

[1] H. M. McConnell and M. Vrljic, Annu. Rev. Biophys. Biomol. Struct. **32**, 469 (2003).
[2] F. Tokumasu, A. J. Jin, G. W. Feigenson, and J. A. Dvorak, Biophys. J. **84**, 2609 (2003).
[3] S. L. Veatch and S. L. Keller, Biophys. J. **85**, 3074 (2003).
[4] S. L. Veatch and S. L. Keller, BBA-Mol. Cell Res. **1746**, 172 (2005).
[5] S. L. Veatch and S. L. Keller, Phys. Rev. Lett. **94**, 148101 (2005).
[6] A. Radhakrishnan, T. G. Anderson, and H. M. McConnell, Proc. Natl. Acad. Sci. U.S.A. **97**, 12422 (2000).
[7] A. Radhakrishnan and H. McConnell, Proc. Natl. Acad. Sci. U.S.A. **102**, 12662 (2005).
[8] S. Mukherjee and F. R. Maxfield, Annu. Rev. Cell Dev. Biol. **20**, 839 (2004).
[9] S. L. Keller and H. M. McConnell, Phys. Rev. Lett. **82**, 1602 (1999).
[10] T. Rog, K. Murzyn, R. Gurbiel, Y. Takaoka, A. Kusumi, and M. Pasenkiewicz-Gierula, J. Lipid Res. **45**, 326 (2004).
[11] M. Pasenkiewicz-Gierula, Y. Takaoka, H. Miyagawa, K. Kitamura, and A. Kusumi, Biophys. J. **76**, 1228 (1999).
[12] G. Brannigan, P. F. Philips, and F. L. H. Brown, Phys. Rev. E **72**, 011915 (2005).
[13] G. Brannigan and F. L. H. Brown, J. Chem. Phys. **120**, 1059 (2004).
[14] G. S. Ayton, J. L. McWhirter, P. McMurtry, and G. A. Voth, Biophys. J. **88**, 3855 (2005).
[15] Q. Du, C. Liu, and X. Q. Wang, J. Comput. Phys. **198**, 450 (2004).
[16] Q. Du, C. Liu, and X. Q. Wang, J. Comput. Phys. **212**, 757 (2005).
[17] W. Helfrich, Z. Naturforsch. C **28**, 693 (1973).
[18] W. T. Gozdz and G. Gompper, Europhys. Lett. **55**, 587 (2001).
[19] J. L. Harden, F. C. MacKintosh, and P. D. Olmsted, Phys. Rev. E **72**, 011903 (2005).
[20] H. Emmerich, *The Diffuse Interface Approach in Materials Science* (Springer, Berlin, 2003).
[21] R. Capovilla, J. Guven, and J. A. Santiago, J. Phys. A **36**, 6281 (2003).
[22] S. L. Wang, R. F. Sekerka, A. A. Wheeler, B. T. Murray, S. R. Coriell, R. J. Braun, and G. B. McFadden, Physica D **69**, 189 (1993).
[23] J. W. Cahn, in *Interfacial Segregation*, edited by W. Johnson and J. Blakely (ASM, Metals Park, OH, 1979), pp. 3–23.
[24] W. C. Johnson, Acta Mater. **49**, 3463 (2001).
[25] G. B. McFadden and A. A. Wheeler, Proc. R. Soc. London, Ser. A **458**, 1129 (2002).
[26] J. Slutsker, K. Thornton, A. L. Roytburd, J. A. Warren, and G. B. McFadden, Phys. Rev. B **74**, 014103 (2006).
[27] W. J. Boettinger, J. A. Warren, C. Beckermann, and A. Karma, Annu. Rev. Mater. Res. **32**, 163 (2002).
[28] K. Thornton, J. Ågren, and P. W. Voorhees, Acta Mater. **51**, 5675 (2003).
[29] R. Capovilla and J. Guven, J. Phys. A **37**, 5983 (2004).
[30] W. Cai and T. C. Lubensky, Phys. Rev. Lett. **73**, 1186 (1994).
[31] F. J. Solis (unpublished).
[32] T. Frankel, *The Geometry of Physics: An Introduction*, 2nd ed. (Cambridge University Press, New York, 2004).